Effect of Land-Use Pattern on the Development of Low-Level Jets

YIHUA WU AND SETHU RAMAN

Department of Marine, Earth and Atmosphere Sciences, North Carolina State University, Raleigh, North Carolina

(Manuscript received 1 April 1996, in final form 8 August 1996)

ABSTRACT

Land-use patterns are a major factor that causes land surface heterogeneities, which in turn influence the development of mesoscale circulations. In the present study, effects of land-use patterns on the formation and structure of mesoscale circulations were investigated using the North Carolina State University mesoscale model linked with the soil–vegetation system. The Midwest type of low-level jet (LLJ) was successfully generated in the model simulation. Characteristics of the LLJ generated in the numerical experiments are consistent with observations. The results suggest that land surface heterogeneities could have significant impacts on the formation and the maintenance of the LLJ.

1. Introduction

Land-use patterns significantly modify physical characteristics of the ground and cause heteorogeneities in the surface features. Their effect on mesoscale atmospheric circulations is due to the generation of horizontal differential heating or strong contrasts in surface thermal fluxes. In many situations, these locally induced circulations are important in determining mesoscale weather conditions. Since the 1980s, the effects of land surface heterogeneity on mesoscale circulations have attracted increased attention. Mahfouf et al. (1987) conducted a simulation of a sea breeze over flat terrain. Their results indicate that the transition zone between bare soil and vegetation is a preferred location for the initiation of moist convection. Segal et al. (1988) showed that strong circulations could develop where contrasts in surface sensible heat fluxes are generated by heterogeneous land surface.

Low-level jets (LLJs) are classified as the meso-β-scale motions with characteristic space scales between 20 and 200 km within the lowest 2 km of the atmosphere, where strong diurnal oscillations and nocturnal accelerations are present. LLJs have been observed in several parts of the world, including southern China (Chen et al. 1994), Japan (Nagata and Ogura 1991), the northwestern part of Germany (Kraus et al. 1985), the Northern Territory of Australia (Brook 1985), eastern Africa (Bannon 1979), and the United States. Among these, the most documented one is the Great Plains LLJ in the middle region of the United States. It is an important element in the low-level atmospheric circulation of this region. It transports water vapor from the Gulf of Mexico and, thus, affects the development of weather over the Great Plains of the central United States. Observations have shown that the Great Plains LLJ is most pronounced in late spring or early summer during periods of ambient southerly flow over the central and southern Great Plains, and it is present over a broad region from the sloping plains just east of the Rocky Mountains to the Mississippi River (Fast et al. 1989; Parish et al. 1987). Bonner's (1968) statistical analysis reveals that LLJs occur predominantly in the Great Plains, with the maximum number occurring over Oklahoma and Kansas. During intensive observation period 4 (IOP 4) at the southern Great Plains Cloud and Radiation Testbed site of the Atmospheric Radiation Measurement program, the LLJ was well observed for 6 days in June 1993 (Fig. 1). Each of the LLJs was associated with nocturnal temperature inversion and had strong diurnal oscillation, forming in the late afternoon or early evening, becoming strongest during the early morning hours of the next day, and then weakening or disappearing by late morning—thus lasting for about 9–12 h. According to the National Ocean and Atmosphere Administration weekly weather summary, powerful storms swept through the nation's midsection, accompanied by tornadoes, high wind, large hail, and heavy rain during the two weeks of 13–19 and 20–26 June 1993. The LLJs appear to have played an important role in these weather events.

The LLJ is generally recognized as a complex response of the atmospheric boundary layer to the diurnal cycle of thermal forcing. Earlier studies have attributed the Great Plains LLJ to 1) the diurnal oscillation of frictional effect (Blackadar 1957), 2) the diurnal oscil-

Corresponding author address: Dr. Sethu Raman, Dept. of Marine, Earth and Atmosphere Sciences, North Carolina State University, Box 8208, Raleigh, NC 27695-8208.
E-mail: s_raman@ncsu.edu

lation of buoyancy over sloping terrain (Holton 1966), and 3) the blocking effects of the Rocky Mountains (Wexler 1961). Recent investigations show that the speed of the LLJ is also affected by the soil type and soil moisture (Fast and McCorcle 1989). Some studies also suggest that synoptic patterns may play an important role in the development of the LLJ (Uccellini 1980; Chen and Kpaeyeh 1992). These investigations of the LLJ have led to a greater understanding of the phenomenon. Yet many important questions about the Great Plains LLJ still remain to be answered. They are as follows. 1) Does the land use pattern affect the development and structure of the LLJ? 2) If so, what is the physical process responsible for this effect? 3) What are the interactive dynamics between the LLJ and the PBL processes? 4) What are the relative roles of the synoptic forcing and the PBL processes in the formation of the LLJ? 5) What is the role of the LLJ in generating and maintaining mesoscale clouds? 6) Last what is the effect of the LLJ on the synoptic-scale circulation? We expect that the heterogeneities of the land surface could have a significant effect on the development and the structure of the LLJ. The main objective of this study is to investigate the effects of land surface heterogeneity on the formation and the structure of the LLJ.

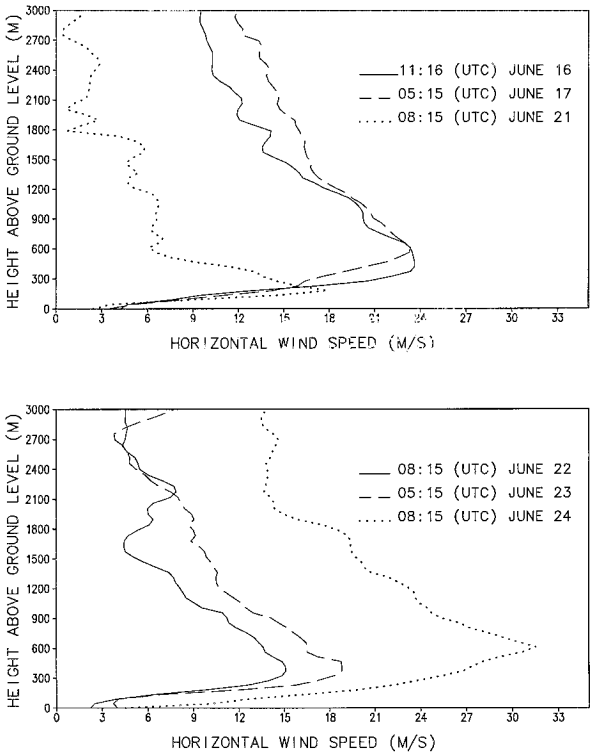

FIG. 1. The low-level jets during 15–25 June 1993 (soundings at Kingman, Kansas).

2. Model description

This study uses the North Carolina State University (NCSU) mesoscale model, which consists of three systems: the atmosphere, the vegetation, and the soil.

a. The atmospheric model

The atmospheric portion of the model is a modified version of the three-dimensional, anelastic, hydrostatic model of the planetary boundary layer originally developed by Huang and Raman (1989, 1991a,b) and Huang and Raman (1990, 1992). The atmospheric PBL is treated as the surface layer (SL) and a transition layer, separately. The SL turbulent transport obeys the similarity stability function given by Businger et al. (1971). Above the SL, prognostic equations for turbulent kinetic energy (TKE) and turbulent dissipation are used. A detailed description of the numerical aspects, including the boundary conditions, is given by Huang and Raman (1991a,b). The numerical scheme used for horizontal advection is a two-time-level, fourth-order Crowley scheme, which uses a free parameter to minimize numerical dispersion and dissipation and, thus, is reliable in representing the advection of positive-definite scalars such as moisture, TKE, and turbulent dissipation. The numerical scheme for vertical advection is a quadratic upstream interpolation scheme, which requires one grid less than the scheme for horizontal advection. The two advection schemes are at least third-order accurate. The original model has been used successfully in several numerical simulations to determine its ability to reproduce known structures of mesoscale circulations under different meteorological conditions and topographic features (Huang and Raman 1990, 1992; Boybeyi and Raman 1992).

b. The soil–vegetation model

The model is linked with the soil–vegetation system to investigate the effects of the surface forcings on mesoscale circulations and the LLJ. The parameterization of the soil–vegetation system is similar to that of Deardorff's (1978). A single layer of vegetation with negligible heat capacity is assumed to be present and is characterized by its physical height, canopy density (shielding factor α_f), optical properties (albedo and emissivity), and stomatal resistance. The foliage surface temperature T_f is determined by the energy budget for the foliage layer. The air temperature and moisture within the canopy are represented by corresponding properties of the air immediately above the canopy, the soil, and the vegetation.

The soil system contains two layers—the top layer is very shallow (10 cm), while the bottom layer is deep (60 cm). The so-called force–restore method is used to calculate the soil surface temperature T_g, which depends on the energy budget at the surface and a restoring term containing the deep soil temperature. The soil surface moisture is estimated in the same way.

TABLE 1. Summary of the numerical experiments.

Cases	Geostrophic wind (m s^{-1})		Land-use pattern
Case 1	$U_g = 0$	$V_g = 0$	Oasis
Case 2	$U_g = 0$	$V_g = 0$	Bare soil–forest contrast
Case 3	$U_g = 0$	$V_g = 10$	Oasis
Case 4	$U_g = 0$	$V_g = 10$	Bare soil–forest contrast

3. Numerical experiments

Four numerical experiments were conducted to determine the effects of land-use patterns on the mesoscale circulations and the LLJ. These four experiments are different combinations of two land-use patterns and two initial wind conditions. A summary of the experiments is given in Table 1. The land-use patterns were prescribed by input parameters such as vegetation type, soil type, soil moisture, and their distribution. Two ideal land-use patterns were chosen in this study. One is the oasis type, which is an area of vegetation within arid surroundings. The other is the contrast of dry bare soil and wet vegetated areas. General surface characteristics of the two land-use patterns are outlined in Table 2. The soil and vegetation input parameters are given in Table 3. The initial profiles of potential temperature and specific humidity used in the simulation are given in Fig. 2. The initial geostrophic wind is southerly, with a speed of 10 m s^{-1} at all levels—that is, $V_g = 10$ m s^{-1}. All the simulations commenced at 0800 LST, which corresponds to the time when sensible heat fluxes become effective in the development of the convective PBL on sunny days. The latitude used in the model is 37.4°N, which is the latitude of Kingman, Kansas. In order to show the diurnal variations of the LLJ, the model was run for a period of 48 h for each simulation. Results from the last 24-h simulation were analyzed.

The model was run in its two-dimensional version in this study. The horizontal domain length was 450 km with a grid spacing of 10 km for case 1 and case 2, and 605 km with a grid spacing of 5 km for case 3 and case 4. The purpose of larger domains in cases 3 and 4 is to ensure that the simulated LLJs are located well within the domain. The vertical domain height is 10 km, with 25 grid points. The vertical grid spacing varies from 30 to 1000 m, with smaller spacing at lower levels. The time step is 10 s.

TABLE 3. Soil and vegetation input parameters. Here, C_v is soil volumetric heat capacity, k soil thermal conductivity, D_h soil thermal diffusivity, z_o roughness length, T soil temperature, Z_a vegetation height, σ_f vegetation shielding factor, $R_{s\,\min}$ minimum stomatal resistance, α_f albedo of the vegetation, and E_f emissivity of the vegetation.

1) Soil	Sand
C_v	1.256×10^6 J m^{-2} K^{-1}
D_h	0.233×10^{-6} m^2 s^{-1}
T	23.8°C
k	0.293 J m^{-1} K^{-1} s^{-1}
z_o	0.01 m
2) Vegetation	Forest
Z_a	10.0 m
$R_{s\,\min}$	100.0 s^{-1}
E_f	0.98
σ_f	0.99
α_f	0.15
z_o	1.0 m

4. Simulation results and discussion

Simulated thermal, turbulent, and dynamic structures of the LLJ for the four experiments, as well as the mechanisms of the LLJ, are shown and discussed in this section. The vegetated regions in the two land-use patterns consist of wet soil (soil moisture is 0.40) and dense forest, with a height of 10 m and a shielding factor of 0.99, while the nonvegetated regions consist of sandy soil, with a soil water content of 0.15. Consequently, soil heat capacity for the vegetated regions is larger than that of the dry bare soil region. Evapotranspiration from the vegetated area is also larger than that from the arid areas. Solar radiation reaching the soil surface in the vegetated areas is substantially less than that reaching the surface in the arid areas. Therefore, the diurnal variation of soil temperature of the arid areas is larger than that of the vegetated areas—that is, daytime and nighttime soil temperatures of the dry bare soil are respectively higher and lower than those of the vegetated soil. This feature, in turn, affects the air temperature near the surface and generates a strong horizontal gradient in sensible heat flux. Thermally induced circulations develop in the transition zone between the bare soil and the vegetated areas due to the horizontal gradient in the sensible heat flux.

TABLE 2. Description of the land-use patterns.

Land-use pattern	Vegetation distribution	Soil moisture (m^3 m^{-3})
Oasis	Case 1: Dry bare soil land, 0–170 km and 300–450 km. Wet forest land, 180–290 km. Case 3: Dry bare soil land, 0–215 km and 390–605 km. Wet forest land, 215–390 km.	0.15 for the bare soil 0.40 for the forest
Bare soil–forest contrast	Case 2: Dry bare soil land, 0–200 km. Wet forest land, 200–450 km. Case 4: Dry bare soil land, 0–415 km, Wet forest land, 415–605.	0.15 for the dry bare soil 0.40 for wet forest

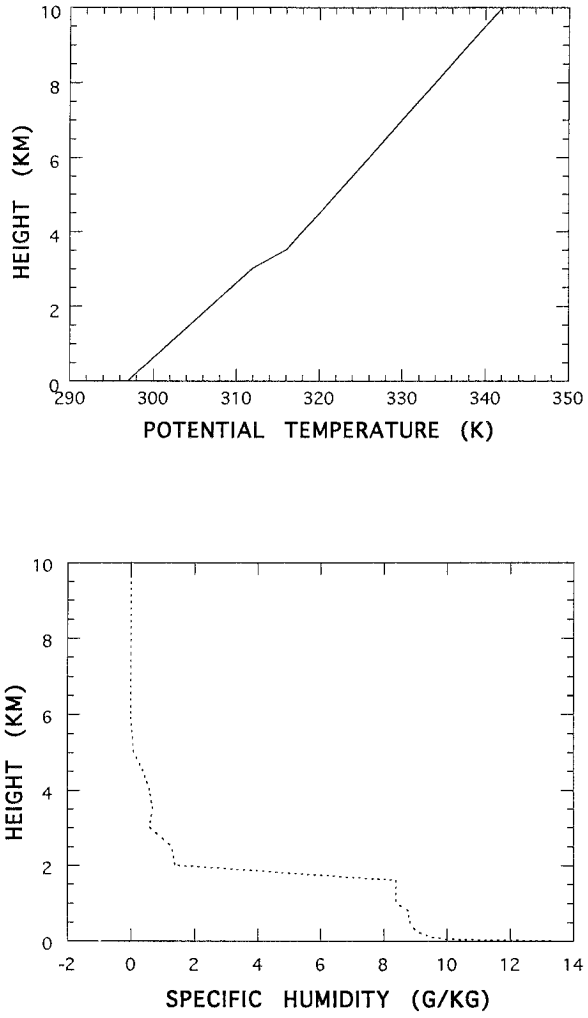

FIG. 2. Vertical profiles of initial temperature and humidity.

a. Case 1—Circulation over the oasis

The model domain consists of three parts: a dry bare soil region extending to a distance of 170 km in the west, a 110-km wet vegetated area located in the center of the model, and another stretch of 170 km of dry bare soil in the east.

1) THERMAL AND TURBULENT STRUCTURE

The *x–z* cross section of predicted potential temperature fields at 1600 LST for the case without geostrophic wind is shown in Fig. 3a. A large difference exists between the air temperatures over the oasis and the arid surroundings. Below 1800 m the potential temperature over the oasis is much cooler than that over the arid surroundings, while between 1800 and 3000 m it is warmer over the oasis. Vertical profiles of potential temperatures at grid points 5, 23, and 41 at 1600 LST are shown in Fig. 3c, where grid points 5 and 41 are two locations in the arid surroundings, while grid point 23 is a location in the oasis. There is a marked difference between the vertical structures of potential temperatures over the oasis and the arid surroundings. The air column between the surface and 2000 m over the oasis can be divided into four layers: a thin superadiabatic layer near the surface, a mixed layer, a strong inversion layer, and a neutral layer. The air between the surface and 2000 m over the surroundings comprises two layers: a superadiabatic layer near the surface and a thick mixed layer. The thin superadiabatic layer is more convective over the arid surroundings than over the oasis, as indicated by the lapse rate. The *x–z* cross section of potential temperature fields at 0400 LST is shown in Fig. 3b. At 0400 LST the entire air column between the surface and 2000 m is very stable over the arid regions, while the four-layer structure of the air column over the oasis is still similar to that predicted for 1600 LST. This difference is clearly seen in the vertical profiles of the potential temperatures of grid points 5, 23, and 41 at 0400 LST in Fig. 3d. Below 150 m the air temperature over the oasis is several degrees warmer than that over the arid regions. A comparison between Fig. 3c and Fig. 3d reveals that the surface temperature and the air temperature near the surface have significant diurnal variations in the surrounding arid regions, but little in the vegetated region.

Because of the large temperature difference between the oasis and its surroundings, a horizontal gradient of sensible heat flux exists. The daytime temperature of the air below 1800 m over the oasis is cooler than that over the arid surroundings. The maximum surface temperature difference is 2.2 K per 10 km at 1600 LST (Fig. 3c). The nighttime temperature of the air below 150 m over the oasis is warmer than that over the surrounding regions due to radiative cooling of the surface. The maximum surface temperature difference is 0.67 K per 10 km at 0400 LST (Fig. 3d).

Simulated TKE distribution is not shown for brevity. A large difference in TKE was predicted over the dry bare soil and vegetation surfaces. During daytime, TKE over the arid surroundings is much larger, with a maximum of 1.30 $m^2\ s^{-2}$, while TKE values over the oasis are close to zero. The boundary layer over the oasis is much thinner than over the dry surroundings. During nighttime, the difference in TKE between the oasis and the surroundings is not as large. The diurnal variation of TKE over the dry surroundings is very significant. TKE values increase from a minimum value (close to zero) around 0900 LST to a maximum (1.3 $m^2\ s^{-2}$) around 1600 LST and then decrease rapidly with time. However, the TKE between 600 and 2100 m still has a value of 0.1–0.2 $m^2\ s^{-2}$ from 1800 to 0300 LST. The diurnal variation of TKE over the oasis, however, is very small.

2) DYNAMIC STRUCTURE

The simulated circulation pattern is shown in Figs. 4 and 5. Simulated vertical motion (the *w* component of

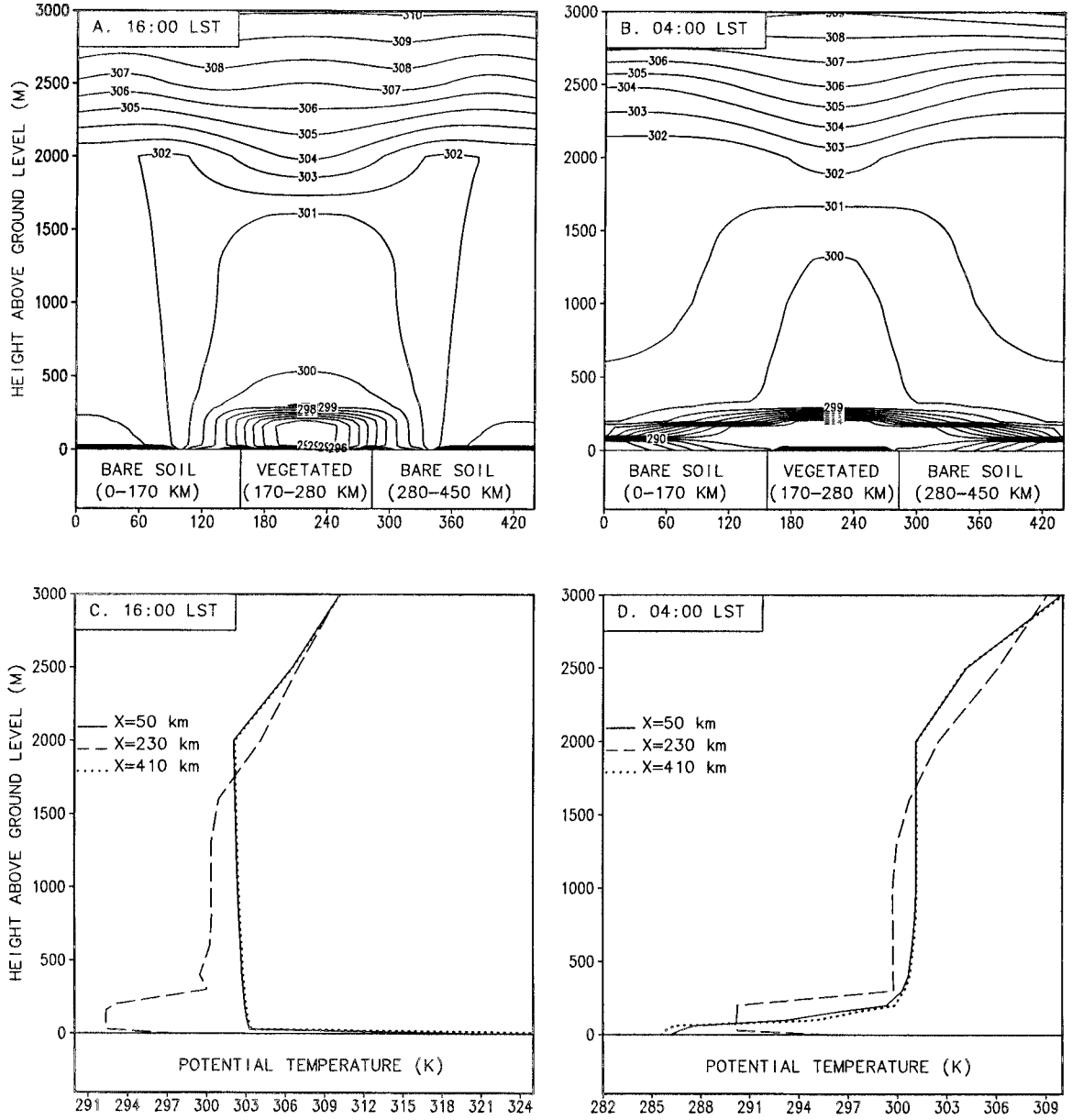

FIG. 3. Potential temperature (PT) (K) in case 1. (a) Spatial distribution of PT at 1600 LST. (b) Spatial distribution of PT at 0400 LST. (c) Vertical profile of PT at grid points 5, 23, and 41 at 1600 LST. (d) Vertical profile of PT at grid points 5, 23, and 41 at 0400 LST.

wind) is shown in Fig. 4, and the predicted horizontal wind speed is shown in Fig. 5. Panels (a) and (b) in these two figures are the z–x cross sections at 1600 and 0400 LST, while panels (c) and (d) are z–time cross sections at grid points 5 and 23 in Fig. 4 and at grid points 8 and 17 in Fig. 5, respectively. As a result of the large horizontal temperature gradient, low-level flow converges from the oasis to the dry surroundings. To conserve the mass, a descending motion develops over the oasis, while ascending motions form over the arid regions surrounding the oasis (Fig. 4). There are two symmetric circulation cells. The maximum magnitudes of the w component and the horizontal wind speed at 1600 LST are greater than 25 cm s^{-1} (Fig. 4a) and 4 m s^{-1} (Fig. 5a), respectively. Vertical motions peak around 1700 LST, with a magnitude of about 26 cm s^{-1} (Figs. 4c,d). At nighttime, the vertical motions decay, especially the descending motion over the oasis, becoming much weaker in magnitude and smaller in extent (Fig. 4b). The magnitude of the w component at 0400 LST is about 8 cm s^{-1}. A pair of maximum horizontal wind speeds develops around 0400 LST below 3000 m (Fig.

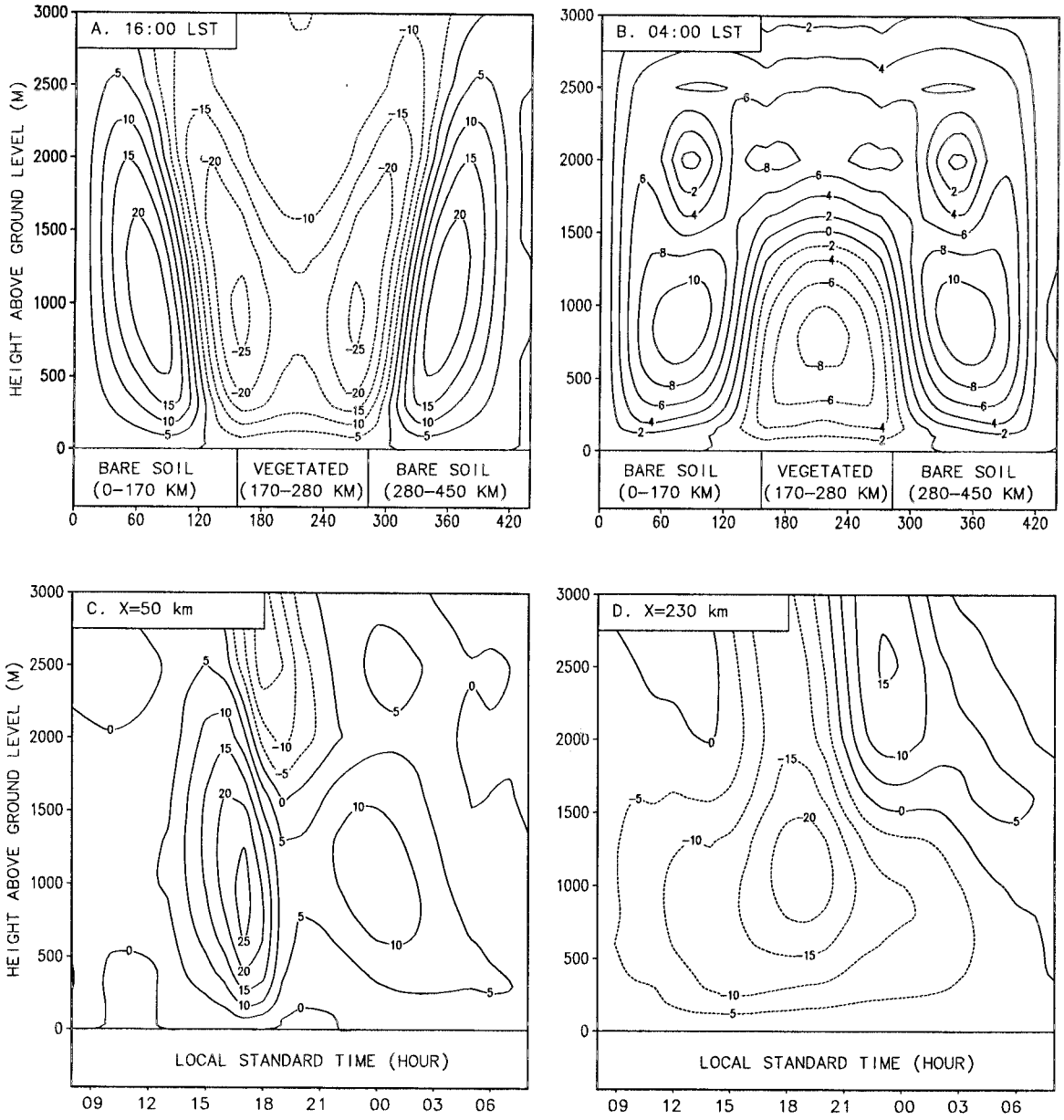

FIG. 4. Vertical motion velocity w (cm s^{-1}) in case 1. (a) Spatial distribution of w at 1600 LST. (b) Spatial distribution of w at 0400 LST. (c) Diurnal variation of w at grid point 5. (d) Diurnal variation of w at grid point 23.

5b)—one pair is at 150 m, and the other is located around 2000 m. Time evolution of this wind structure is shown by the z–time cross section at grid points 8 and 17 (Figs. 5c,d). These grid points correspond to the locations of the western pair of wind maxima in the model domain (Fig. 5b). The horizontal wind speed in the transition zone between the oasis and the arid regions changes diurnally, winds at 200 m reach their peak (7 m s^{-1}) around 2100 LST (Fig. 5c), while winds at 2000 m reach their peak (5 m s^{-1}) around 0300 LST (Fig. 5d). These local wind maxima could augment any pre-existing LLJ that forms under favorable synoptic conditions.

b. Case 2—Circulation in the simulation of bare soil–vegetated soil contrast

In this case, the model domain consists of only two parts: a dry bare soil region of 200 km in the west and a wet dense forest region of 250 km in the east. Compared with the oasis type, this type of land-use pattern

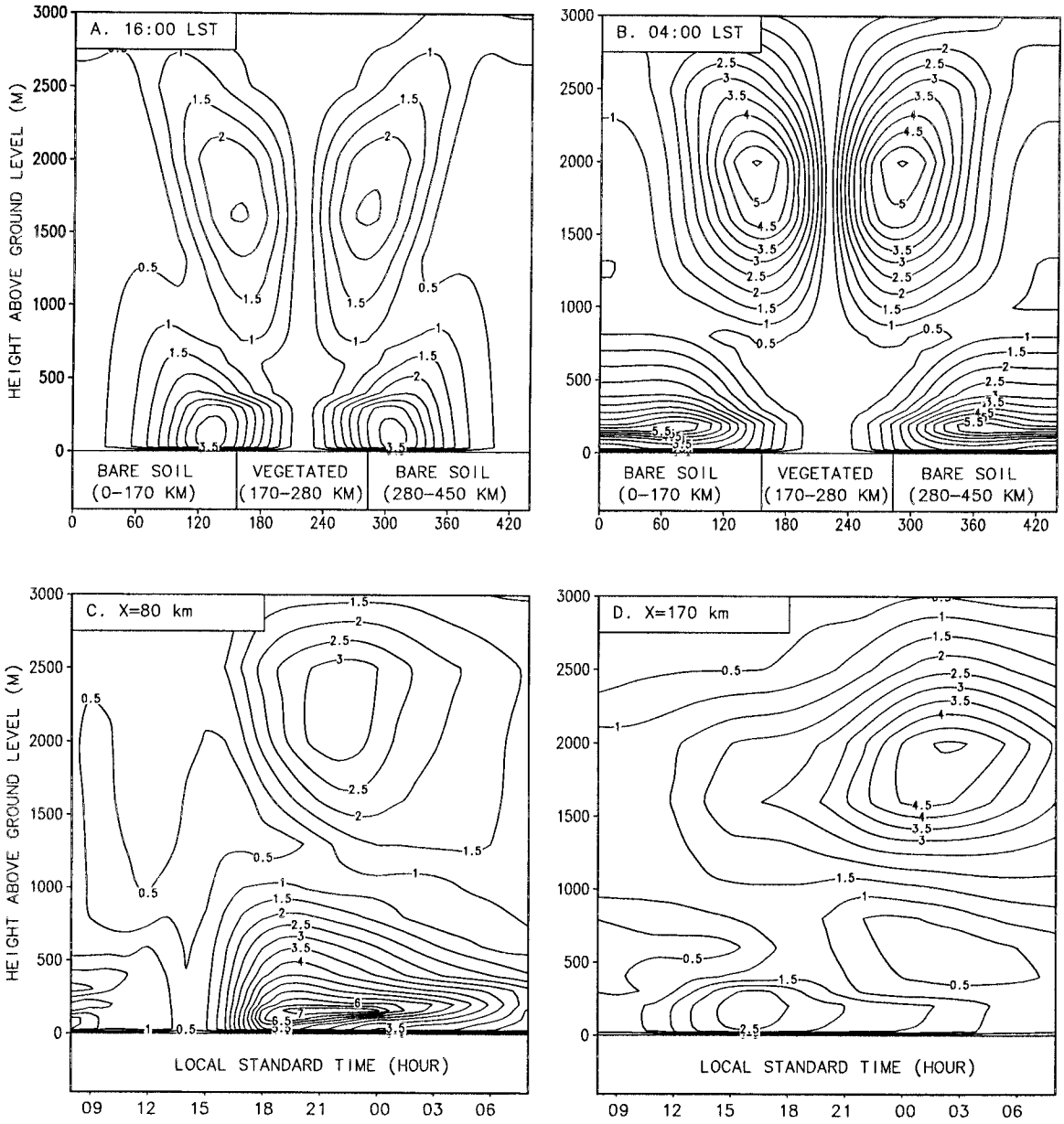

FIG. 5. Horizontal wind speed (HWS) (m s^{-1}) in case 1. (a) Spatial distribution of HWS at 1600 LST. (b) Spatial distribution of HWS at 0400 LST. (c) Diurnal variation of HWS at grid point 8. (d) Diurnal variation of HWS at grid point 17.

is more common in summer agricultural land-use regions.

1) THERMAL AND TURBULENT STRUCTURE

Simulated temperature fields at 1600 and 0400 LST are given in Fig. 6. Figures 6a and 6b are z–x cross sections of potential temperature at 1600 and 0400 LST. Figures 6c and 6d are the vertical profiles of potential temperature at grid point 10 (a location in the bare soil region) and grid point 35 (a location in the vegetated region). A large difference in potential temperature exists between the dry bare soil region and the wet dense forest region. The air temperatures below and above 1800 m over the dry bare soil region are, respectively, several degrees warmer and cooler than those over the vegetated region during daytime (Figs. 6a,c). However, at night, the air temperature below 100 m over the forest region is warmer than that over the dry bare soil region (Figs. 6b,d).

The difference in simulated TKEs over the dry bare soil and the wet forest is also significant in this case (not shown). During daytime, TKE (and hence turbulence) is larger over the dry soil region (with a maximum

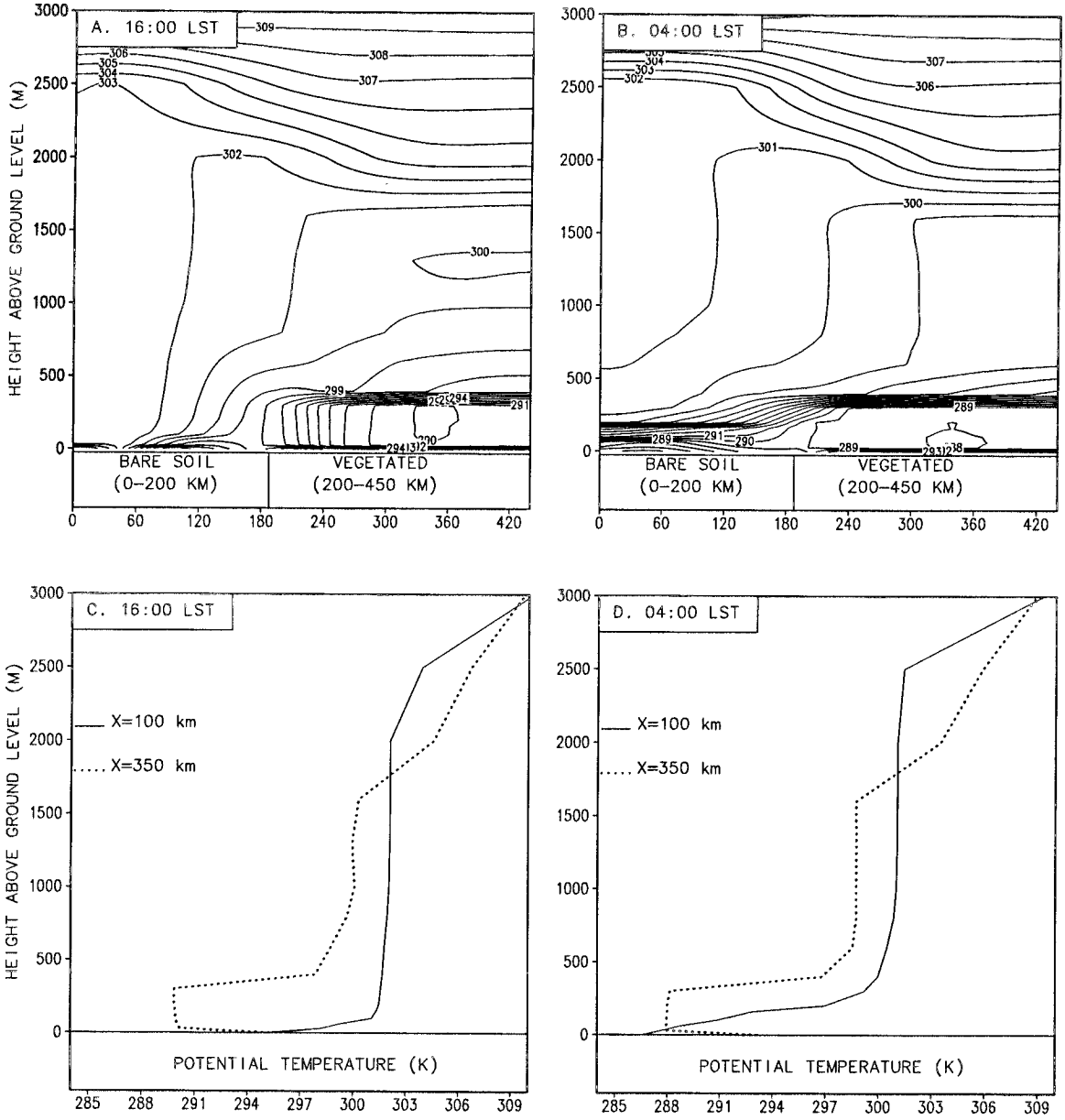

FIG. 6. Potential temperature (PT) (K) in case 2. (a) Spatial distribution of PT at 1600 LST. (b) Spatial distribution of PT at 0400 LST. (c) Vertical profile of PT at grid points 10 and 35 at 1600 LST. (d) Vertical profile of PT at grid points 10 and 35 at 0400 LST.

of 0.4 $m^2 s^{-2}$) than over the forest region (with a maximum of 0.1 $m^2 s^{-2}$). At night, little difference exists between the bare soil region and the vegetated soil region. The diurnal variation of TKE is more significant over the dry soil region than over the forest region.

2) DYNAMIC STRUCTURE

Spatial structure and the time evolution of the simulated circulation are shown by vertical motion (Fig. 7) and horizontal wind speed (Fig. 8). One cell pattern of circulation develops due to the horizontal temperature difference. During daytime, the dry soil heats up more quickly and the low-level flow circulates from the forest region to the dry bare soil region. In order to conserve the air mass, ascending and descending motions develop, respectively, over the dry bare soil region and the forest region (Fig. 7). The circulation has a diurnal cycle. The ascending air has a maximum speed of about 24 cm s^{-1} at 1600 LST (Fig. 7a) and greater than 14 cm s^{-1} at 0400 LST (Fig. 7b). The descending air has a maximum speed of about 12 cm s^{-1} at 1600 LST (Fig.

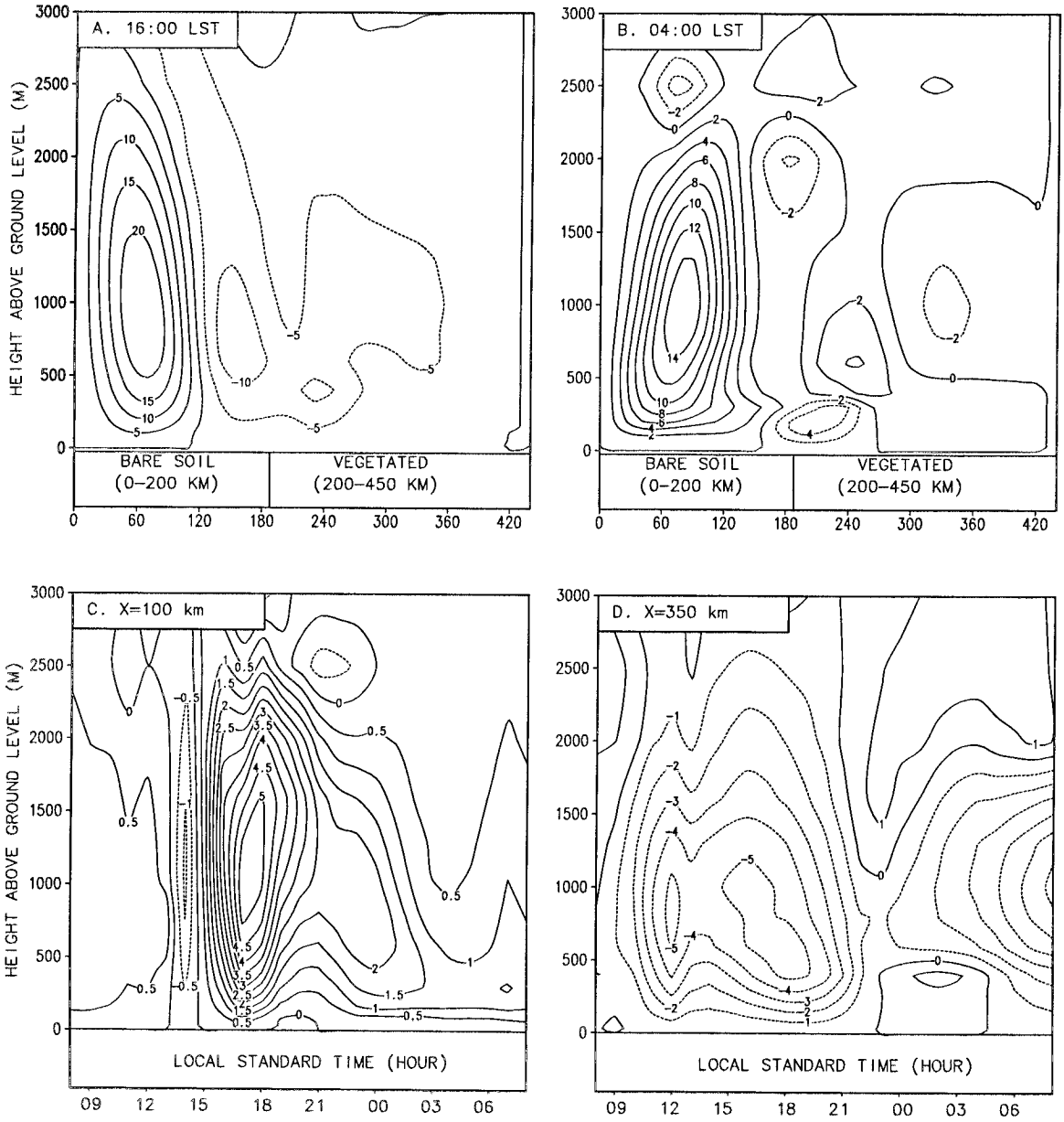

FIG. 7. Vertical motion velocity (w) (cm s^{-1}) in case 2. (a) Spatial distribution of w at 1600 LST. (b) Spatial distribution of w at 0400 LST. (c) Diurnal variation of w at grid point 10. (d) Diurnal variation of w at grid point 35.

7a) and 4 cm s^{-1} at 0400 LST (Fig. 7b). This diurnal variation of both ascending and descending motions is also apparent in the z–time cross sections of the vertical motion (Figs. 7c,d) at grid points 10 and 35. By late night, the circulation changes its direction due to the reversal of surface temperature difference (data not shown). Two regions of maximum winds are clearly displayed in the horizontal wind field at 1600 LST and 0400 LST (Figs. 8a,b). One is located at 250 m and the other at 2000 m. To show the diurnal variation of the two maximum wind regions, z–time cross sections at grid points 14 and 23 are plotted in Figs. 8c,d. A maximum wind region begins to form around 1400 LST at lower levels, reaches a peak intensity (7 m s^{-1}) around 1700 LST, and starts to disappear around 0200 LST. The maximum wind region at upper levels begins to form around 0000 LST, reaches its peak (5 m s^{-1}) around 0400 LST, and starts to disappear by 1500 LST.

c. Case 3—The LLJ over the oasis

In this case, the horizontal domain length is 605 km, larger than that in case 1. Widths of the dry bare soil regions in the west and in the east are 215 km, while

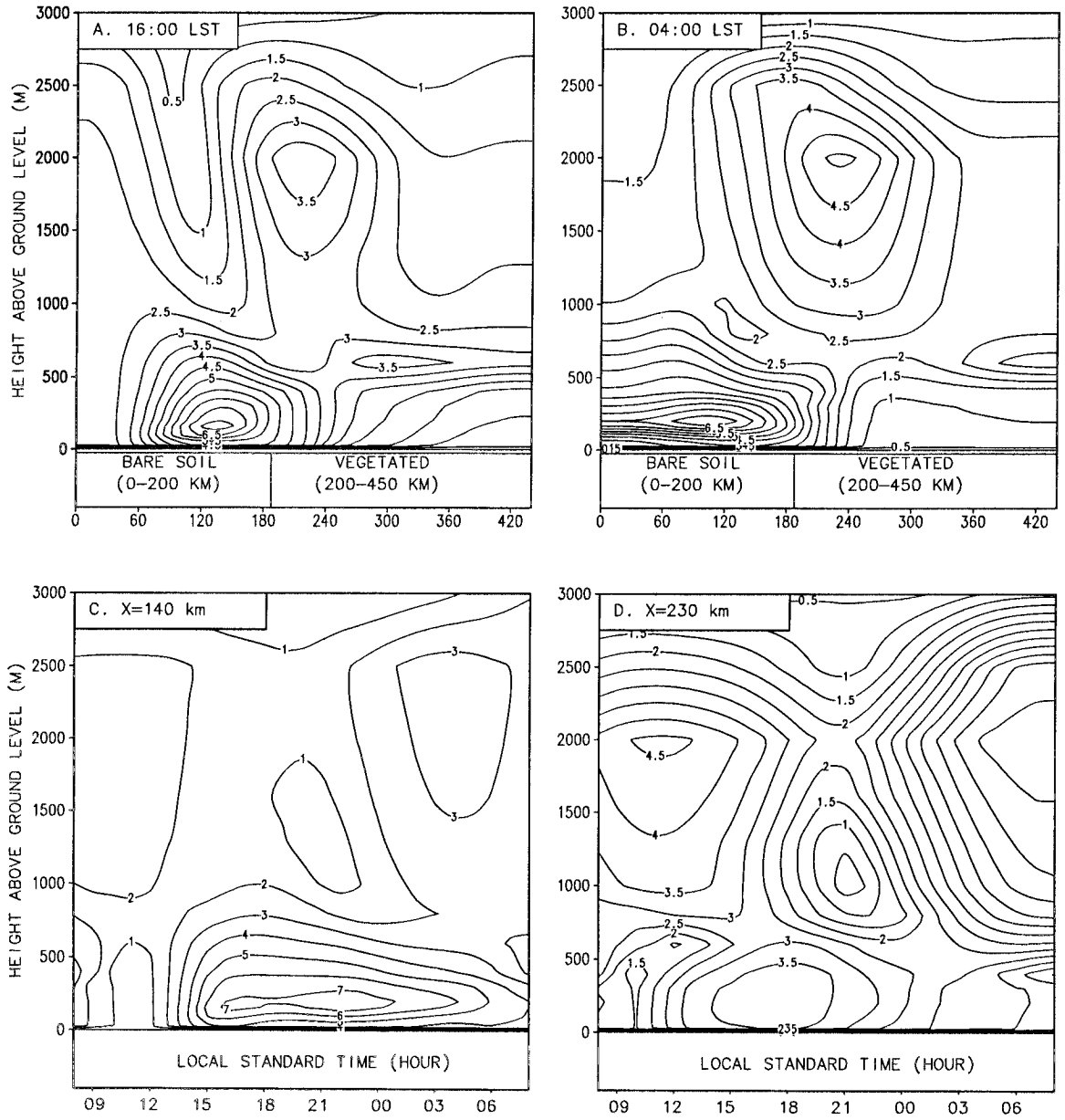

FIG. 8. Horizontal wind speed (m s^{-1}) in case 2. (a) Spatial distribution of HWS at 1600 LST. (b) Spatial distribution of HWS at 0400 LST. (c) Diurnal variation of HWS at grid point 14. (d) Diurnal variation of HWS at grid point 23.

the width of the vegetated region in the center is 175 km.

1) THERMAL AND TURBULENT STRUCTURE

The simulated potential temperatures for the case with a southerly geostrophic wind of 10 m s^{-1} are given in Fig. 9. As in case 1, a large difference exists between the potential temperatures over the oasis and the arid surroundings. However, the pattern of the potential temperature field is not as symmetric (Figs. 9a,b). The maximum surface temperature difference between the oasis and its surroundings at 1600 LST is about 29 K (Fig. 8c), smaller than that in case 1 (about 35 K). The difference in near-surface air temperature over the oasis and the surroundings is about 8 K, also smaller than that in case 1 (10 K). At 0400 LST, the difference between the near-surface air temperatures is less in this case than in case 1 (Fig. 9d). A comparison between Fig. 9c and Fig. 9d shows that the surface temperature and the low-level air temperature have a significant diurnal variation in the arid surrounding regions, but little in the vegetated region. As indicated by TKE values (data not shown), the boundary layer heights over both

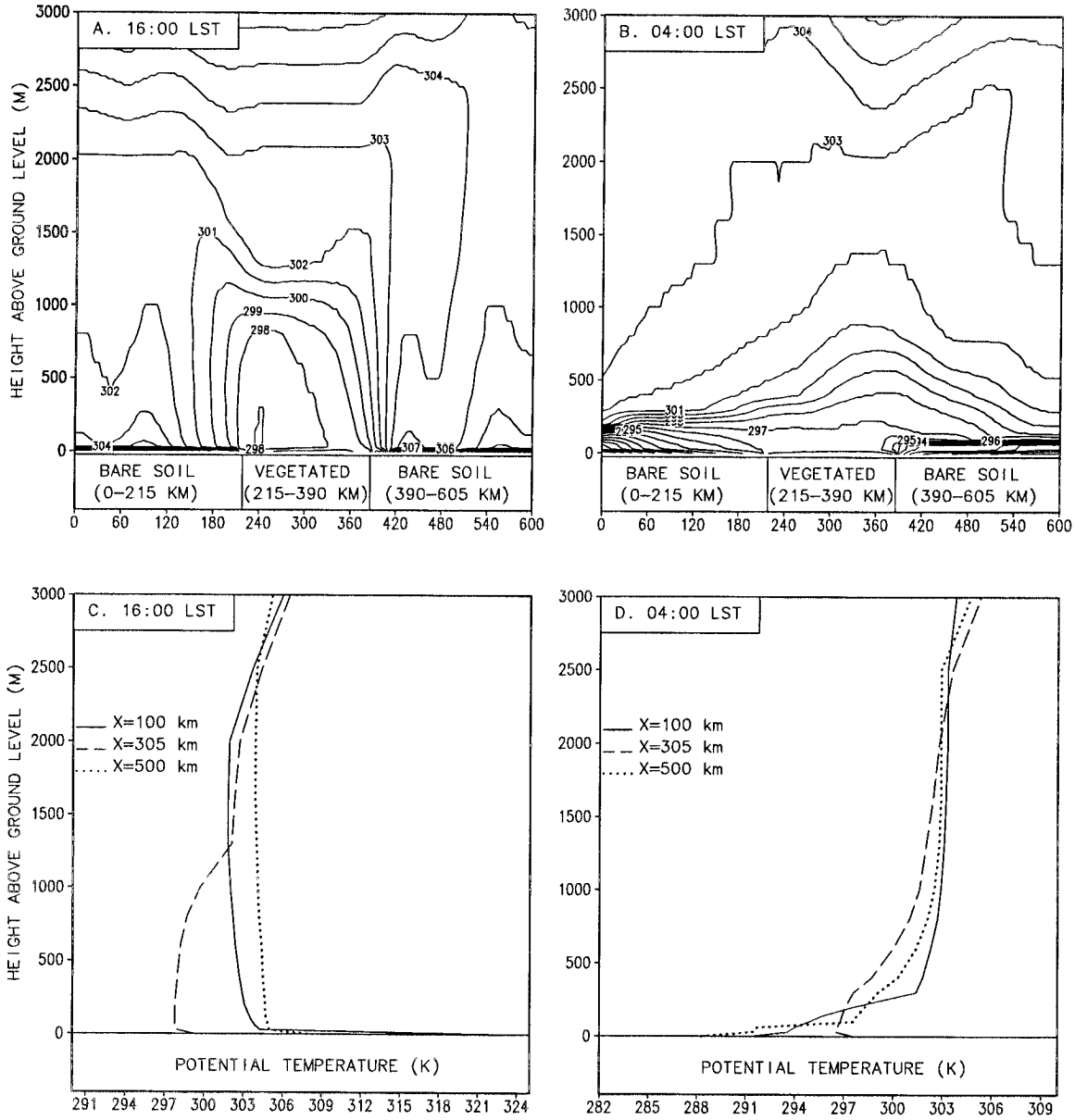

FIG. 9. Potential temperature (K) in case 3. (a) Spatial distribution of PT at 1600 LST. (b) Spatial distribution of PT at 0400 LST. (c) Vertical profile of PT at grid points 20, 61, and 100 at 1600 LST. (d) Vertical profile of PT at grid points 20, 61, and 100 at 0400 LST.

the oasis and the dry surroundings and their diurnal variations are very similar to those in case 1. However, the TKE values in this case are larger, with a maximum of 3.6 $m^2 s^{-2}$, indicating stronger turbulence. The values of TKE have significant diurnal oscillations over the arid surroundings, but little over the oasis.

2) DYNAMIC STRUCTURE

The dynamic structure of the simulated circulation is shown by the vertical motion (Fig. 10) and horizontal wind speed (Fig. 11). As described in the previous section, panels (a) and (b) in these two figures are *z–x* cross sections at 1600 and 0400 LST, while panels (c) and (d) are *z–t* cross sections at two particular points, which, in this case, are grid points 24 and 61 in Fig. 10 and grid points 24 and 96 in Fig. 11, respectively. The two-cell circulation pattern in this case is considerably distorted. Vertical motions are stronger in this case than in case 1. At 1600 LST (Fig. 10a), the vertical motions at the right transition zone are much stronger than those at the left transition zone. The maximum magnitude of the *w* component is about 30 cm s^{-1} at 1600 LST. At 0400 LST (Fig. 10b) vertical motions are much weaker than that at

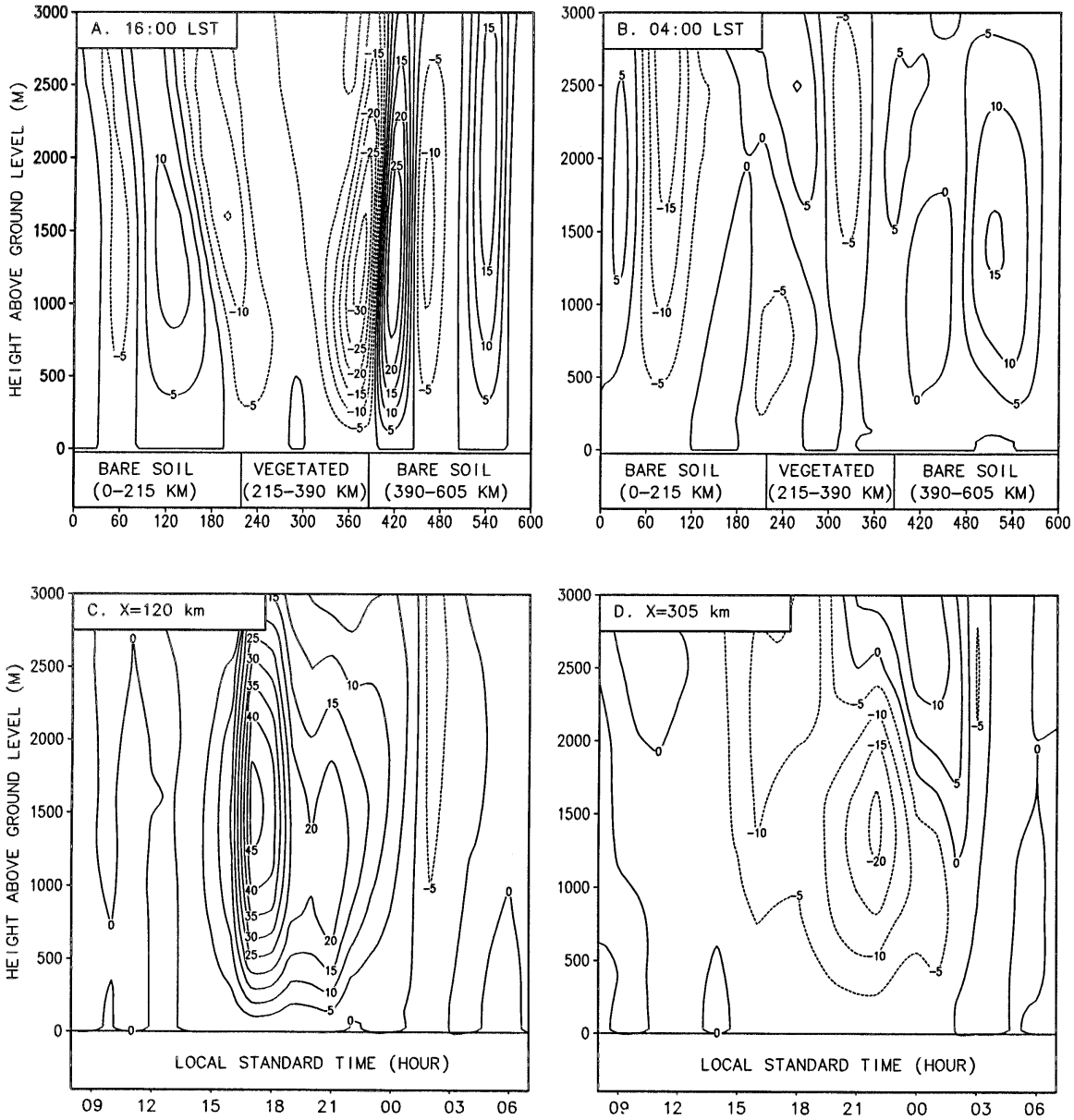

FIG. 10. Vertical motion velocity w (cm s^{-1}) in case 3. (a) Spatial distribution of w at 1600 LST. (b) Spatial distribution of w at 0400 LST. (c) Diurnal variation of w at grid point 24. (d) Diurnal variation of w at grid point 61.

1600 LST. Diurnal variation of the vertical motions can be seen by comparing Fig. 10a (1600 LST) and Fig. 10b (0400 LST). Figures 10c,d show the temporal variation of vertical velocity at grid point 24 over the dry bare soil and at grid point 61 over the oasis, respectively. Diurnal variation can be seen in both locations. At grid point 24, between 0000 and 0300 LST, the air descends. However, between 1500 and 0000 LST, the air ascends at this location. Large vertical motion occurs between 1500 and 0000 LST, with a maximum of 45 cm s^{-1} at about 1700. While at grid point 61, large vertical motion occurs between 2100 and 0000 LST with a maximum of 20 cm s^{-1}. Horizontal wind speeds at 1600 LST are shown in Fig. 11a. At this time, horizontal wind speeds at upper levels are much stronger than that near the surface. Two LLJs are predicted and are apparent in the horizontal wind field at 0100 LST—one located at a height of 200 m and the other at 1800 m (Fig. 11b). To show the time evolution of the LLJs, z–time cross sections of horizontal wind speed at grid points 24 and 96 are given in Fig. 11c and Fig. 11d, respectively. The jet at 200 m forms around 2200 LST, reaches its peak (14.5 m s^{-1}) at approximately 0200 LST, and lasts for about 10 h. The LLJ reached the lateral boundary of the model domain at later stages. The jet at 1800 m is not apparent in Fig. 11d because of its transient nature.

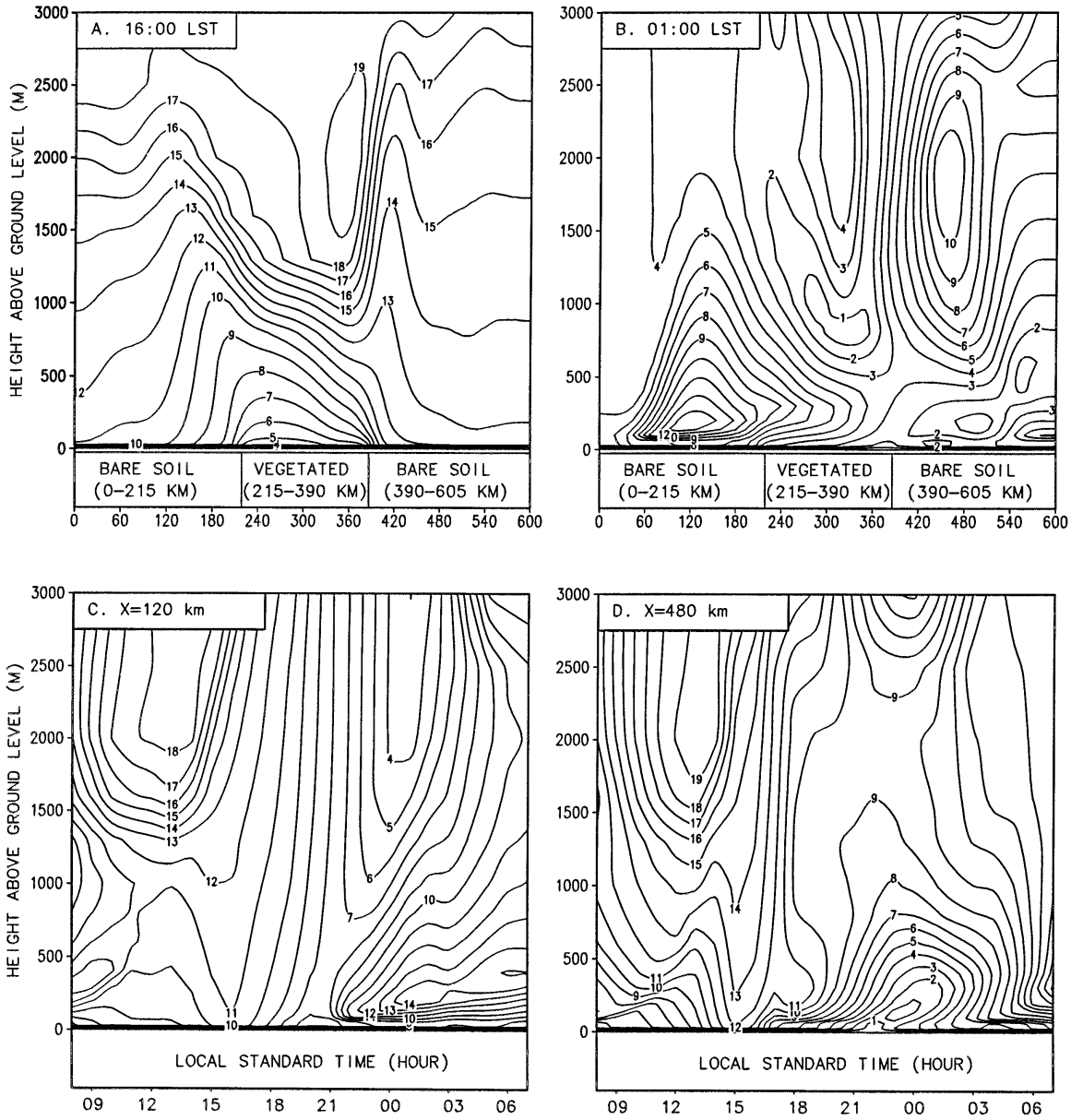

FIG. 11. Horizontal wind speed (m s^{-1}) in case 3. (a) Spatial distribution of HWS at 1600 LST. (b) Spatial distribution of HWS at 0100 LST. (c) Diurnal variation of HWS at grid point 24. (d) Diurnal variation of HWS at grid point 96.

d. Case 4—The LLJ in the simulation of bare soil–vegetated soil contrast

The horizontal domain length is 605 km in this case, with a dry bare soil region of 355 km in the west and a wet vegetated region of 250 km in the east.

1) THERMAL AND TURBULENT STRUCTURE

In this simulation, daytime air temperature below 1200 m is about 5 K warmer over the dry soil region than over the forest, while nighttime air temperature near the surface in the forest region is several degrees warmer than over the bare soil region (Figs. 12a,b). At 1600 LST the surface temperature is about 35 K warmer in the dry bare soil region than in the vegetated region, while at 0400 LST the surface temperature is about 3 K cooler in the dry bare soil region than in the vegetated region (Figs. 12c,d). The spatial distribution pattern and time evolution of TKE are similar to those in case 2, but the magnitude is larger, with a maximum of 2.0 m^2 s^{-2} during daytime and 0.7 m^2 s^{-2} at nighttime.

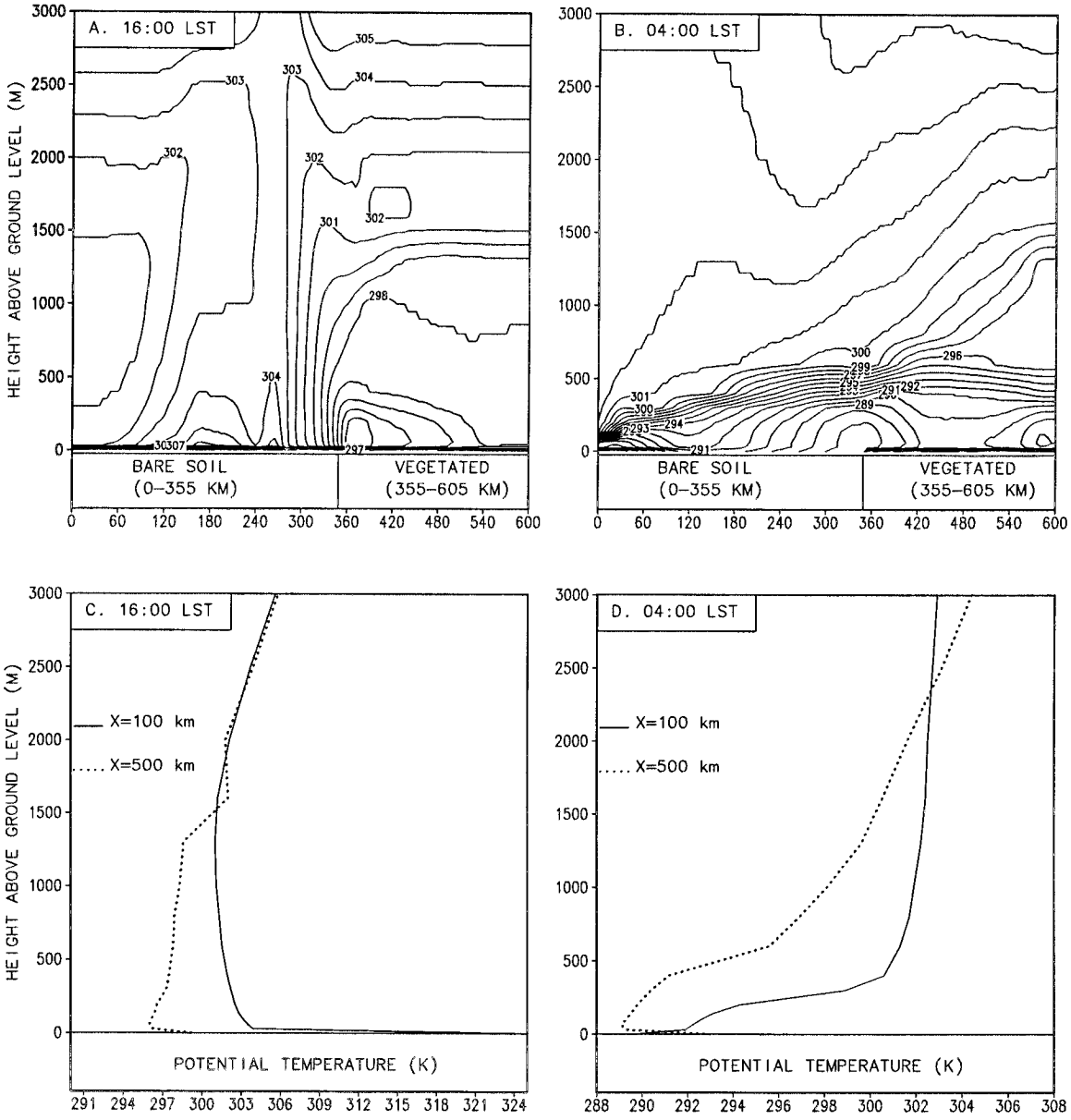

FIG. 12. Potential temperature (K) in case 4. (a) Spatial distribution of PT at 1600 LST. (b) Spatial distribution of PT at 0400 LST. (c) Vertical profile of PT at grid points 20 and 100 at 1600 LST. (d) Vertical profile of PT at grid points 20 and 100 at 0400 LST.

2) DYNAMIC STRUCTURE

The circulation pattern in this case (Figs. 13 and 14) is similar to that in case 2, but is much stronger. At 1600 LST the strongest vertical motions occur in the transition zone between the bare soil and vegetated regions. The maximum ascending speed is about 35 cm s^{-1}, while the maximum descending speed is about 15 cm s^{-1} (Fig. 13a). At 0400 LST vertical motion in the transition zone is very weak (Fig. 13b). The vertical motions have significant diurnal variation, as indicated by both the magnitude of the vertical motion and its extension. The temporal variations of vertical velocity at grid point 36 over the dry bare soil region and grid point 100 over the vegetated region are shown in Figs. 13c and 13d. The diurnal variation of vertical motions is much stronger at grid point 36 than at grid point 100. No LLJ structure is shown in the horizontal wind speeds at 1600 LST (Fig. 14a). At 0100 LST a low-level jet structure can be seen in the horizontal wind field (Fig. 14b). The maximum speed is located at the 400-m level. The LLJ formed around 2000 LST, reached its peak (19 m s^{-1}) around 0300 LST, and began to disappear by 0900 LST. It thus lasted for about 10 h (Fig. 14c).

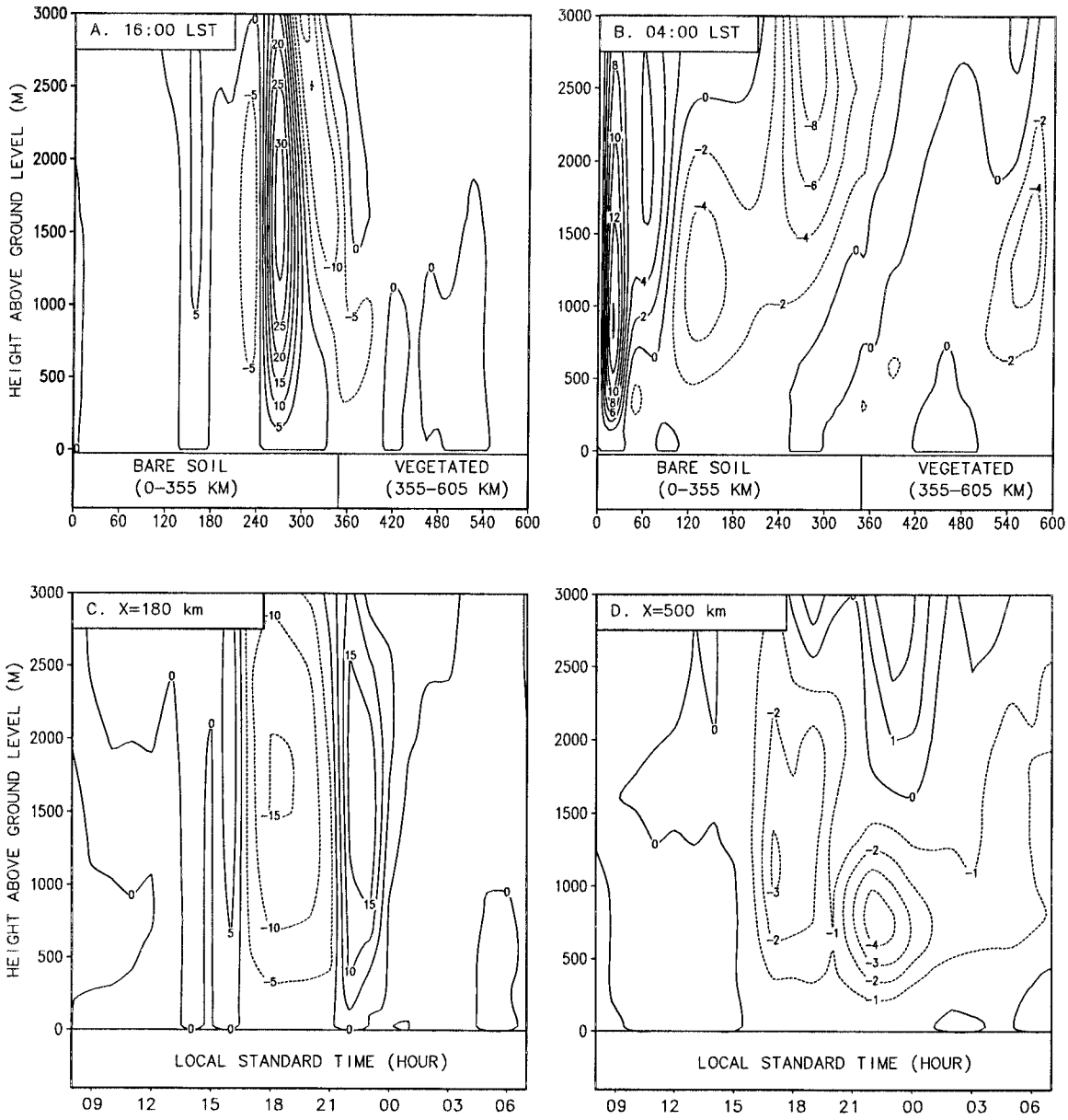

FIG. 13. Vertical motion velocity w (cm s^{-1}) in case 4. (a) Spatial distribution of w at 1600 LST. (b) Spatial distribution of w at 0400 LST. (c) Diurnal variation of w at grid point 36. (d) Diurnal variation of w at grid point 100.

As shown in Figs. 14c and 14d, there is an oscillation in the horizontal wind speed up to a height of 4500 m. This is believed to be due to diurnal variation of air temperatures at these levels caused by the mesoscale motions induced by surface heterogeneities. Similar results were obtained for case 3 (not shown).

e. Important mechanisms of the LLJ

To gain insight into the important mechanisms that produce or enhance the LLJs in cases 3 and 4, we start with momentum equations for the east–west and north–south wind components u and v, respectively. The two equations in the model are of the following form:

$$\frac{\partial u}{\partial t} = -u\frac{\partial u}{\partial x} - v\frac{\partial u}{\partial y} - \tilde{w}\frac{\partial u}{\partial \sigma} + fv - \theta_v\frac{\partial \pi}{\partial x} - g(1-\sigma)\frac{\partial \hat{E}}{\partial x} + \frac{\partial}{\partial x}\left(K\frac{\partial u}{\partial x}\right) + \frac{\partial}{\partial y}\left(K\frac{\partial u}{\partial y}\right) + \frac{1}{H-\hat{E}}\frac{\partial(\overline{-u'w'})}{\partial \sigma} \quad (1)$$

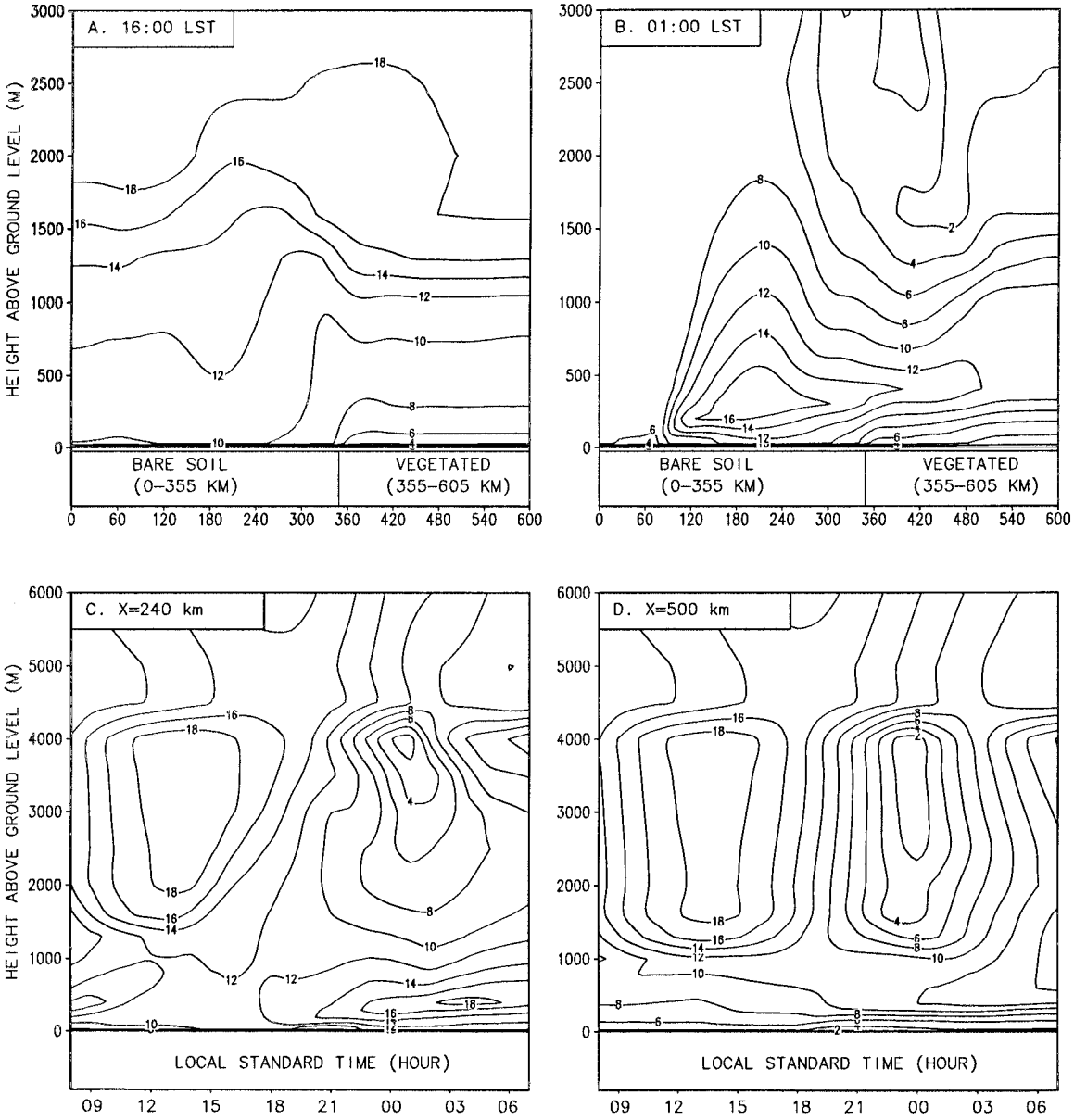

FIG. 14. Horizontal wind speed (m s^{-1}) in case 4. (a) Spatial distribution of HWS at 1600 LST. (b) Spatial distribution of HWS at 0100 LST. (c) Diurnal variation of HWS at grid point 48. (d) Diurnal variation of HWS at grid point 100.

$$\frac{\partial v}{\partial t} = -u\frac{\partial v}{\partial x} - v\frac{\partial v}{\partial y} - \tilde{w}\frac{\partial v}{\partial \sigma} - fu - \theta_v\frac{\partial \pi}{\partial y} - g(1-\sigma)\frac{\partial \hat{E}}{\partial y} + \frac{\partial}{\partial x}\left(K\frac{\partial v}{\partial x}\right) + \frac{\partial}{\partial y}\left(K\frac{\partial v}{\partial y}\right) + \frac{1}{H-\hat{E}}\frac{\partial(\overline{-v'w'})}{\partial \sigma}, \quad (2)$$

where u is the eastward moving wind component, v the northward moving wind component, u' the fluctuation of u, v' the fluctuation of v, w' the fluctuation of the upward moving wind component, K the eddy diffusivity for momentum, f the Coriolis parameter, ρ the air density, p the atmospheric pressure, $\hat{E}$ the terrain height, and H the constant height of the model domain, and where σ is defined as $\sigma = [z - \hat{E}(x, y)]\,[H - \hat{E}(x, y)]^{-1}$.

As shown by Holton (1966) and Clark (1987), the sloping terrain is important in the formation of the LLJ. However, in this study, we will only focus on the effect of land-use patterns on the LLJ. Therefore, the terrain is not considered in this study.

When terrain height is zero, the two momentum equations can be rewritten as

$$\frac{du}{dt} = fv - \frac{1}{\rho}\frac{\partial p}{\partial x} + \frac{\partial}{\partial x}\left(K\frac{\partial u}{\partial x}\right) + \frac{\partial}{\partial y}\left(K\frac{\partial u}{\partial y}\right) - \frac{\overline{\partial(-u'w')}}{\partial z} \tag{3}$$

and

$$\frac{dv}{dt} = -fu - \frac{1}{\rho}\frac{\partial p}{\partial y} + \frac{\partial}{\partial x}\left(K\frac{\partial v}{\partial x}\right) + \frac{\partial}{\partial y}\left(K\frac{\partial v}{\partial y}\right) - \frac{\overline{\partial(-v'w')}}{\partial z}. \tag{4}$$

Although the boundary layer winds are rarely geostrophic, the definition of the geostrophic wind can be used as a substitute variable for the horizontal pressure gradient terms:

$$fu_g = -\frac{1}{\rho}\frac{\partial P}{\partial x} \quad \text{and} \quad fv_g = \frac{1}{\rho}\frac{\partial P}{\partial y}.$$

Thus, the horizontal components of Eqs. (3) and (4) become

$$\frac{du}{dt} = fv - fv_g + \frac{\partial}{\partial x}\left(K\frac{\partial u}{\partial x}\right) + \frac{\partial}{\partial y}\left(K\frac{\partial u}{\partial y}\right) - \frac{\overline{\partial(-u'w')}}{\partial z} \tag{5}$$

and

$$\frac{dv}{dt} = -fu + fu_g + \frac{\partial}{\partial x}\left(K\frac{\partial v}{\partial x}\right) + \frac{\partial}{\partial y}\left(K\frac{\partial v}{\partial y}\right) - \frac{\overline{\partial(-v'w')}}{\partial z}. \tag{6}$$

Assuming that friction suddenly disappears above the surface layer at sunset (Blackadar 1957; Stull 1988) and remains zero through the night, and that geostrophic wind is independent of time, Eqs. (5) and (6) become

$$\frac{d}{dt}(u - u_g) = f(v - v_g) \tag{7}$$

and

$$\frac{d}{dt}(v - v_g) = -f(u - u_g). \tag{8}$$

Letting $V_d = (u - u_g) + i(v - v_g)$ and combining Eqs. (7) and (8),

$$\frac{dV_d}{dt} = -ifV_d. \tag{9}$$

With $V_d^0 = (u^0 - u_g^0) + i(v^0 - v_g^0)$, the solution for Eq. (9) will be of the form

$$u = u_g + (u^0 - u_g^0)\cos(ft) + (v^0 - v_g^0)\sin(ft) \tag{10}$$

and

$$v = v_g - (u^0 - u_g^0)\sin(ft) + (v^0 - v_g^0)\cos(ft), \tag{11}$$

where u^0 and v^0 are east–west and north–south components of wind at sunset, and u_g^0 and v_g^0 are east–west and north–south components of geostropic wind at sunset.

Based on hydrostatic equilibrium, the geostrophic wind must have vertical shear in the presence of a horizontal temperature gradient. The equations for the change of the geostrophic wind components with height in the z-coordinate system are of the form

$$u_g = u_{g1} - \frac{g(z - z_1)}{f\overline{T}}\frac{\partial \overline{T}}{\partial y} \tag{12}$$

and

$$v_g = v_{g1} + \frac{g(z - z_1)}{f\overline{T}}\frac{\partial \overline{T}}{\partial x}, \tag{13}$$

where $\overline{T}$ denotes the mean temperature in the layer between height z_1 and z, and u_{g1} and v_{g1} are the geostrophic wind components at the level z_1. Substituting Eqs. (12) and (13) in Eqs. (10) and (11), respectively, we get

$$u = u_{g1} - \frac{g(z - z_1)}{f\overline{T}}\frac{\partial \overline{T}}{\partial y} + (u^0 - u_g^0)\cos(ft) + (v^0 - v_g^0)\sin(ft) \tag{14}$$

and

$$v = \underbrace{v_{g1}}_{1} + \underbrace{\frac{g(z - z_1)}{f\overline{T}}\frac{\partial \overline{T}}{\partial x}}_{2} - \underbrace{(u^0 - u_g^0)\sin(ft) + (v^0 - v_g^0)\cos(ft)}_{3}. \tag{15}$$

From Eqs. (14) and (15) it is apparent that the PBL winds at night depend on three terms: the geostrophic wind at z_1, the mean horizontal temperature gradient between z_1 and z, and the oscillation about the geostrophic value. However, we have assumed the geostrophic wind at z_1 to be constant. Therefore, the mean horizontal temperature gradient and the inertial oscillation–frictional effect are the two mechanisms for the occurrence of the LLJs in cases 3 and 4. The magnitude of the oscillation at night depends on the amount of geostrophic departure at the end of the day, $(u^0 - u_g^0)$ and $(v^0 - v_g^0)$. The second term in Eqs. (14) and (15) varies diurnally due to heating and cooling of the surface and due to land surface heterogeneities, although it is not shown as a function of time in the equations. For case 3 (Fig. 9d) air temperature below 200 m over the oasis is about 5 K warmer than that over the dry bare soil region to the west. This horizontal temperature gradient is one of the two major forcings for the jet at 200 m. In case 4 (Fig. 12d) the air temperature near the surface is larger over the forest than over the bare soil.

This horizontal temperature gradient is thus a major factor for the formation of the LLJ at 300 m.

5. Conclusions

The effects of land-use patterns on the formation and development of mesoscale circulations, especially the LLJ, were investigated using the NCSU numerical model linked with a soil–vegetation system. Two ideal land-use patterns were chosen in this study—one is the oasis type and the other is the contrast of dry bare soil and wet vegetated areas. Two different environmental flows were also chosen—one was assumed to be a negligible synoptic flow and the other a southerly geostrophic flow. This idealized numerical study reveals many important features of LLJs and the mechanisms of their development. 1) The effect of land-use patterns on mesoscale circulations is significant when large land surface heterogeneities exist. A thermal circulation that is comparable to sea breeze in intensity is generated in the transition zone between bare soil and vegetated regions for a weak synoptic flow, while much stronger circulation occurs with a southerly geostrophic flow. 2) A well-defined jet occurs at nights for both cases. 3) The circulations and the LLJ have significant diurnal variation. The major mechanisms for the LLJ are the horizontal temperature gradient caused by land surface heterogeneities and the oscillation of the frictional effect. The southerly geostrophic wind is also a necessary condition for the LLJ. Although the simulated LLJs are for ideal conditions, they are similar to the observed ones in their significant diurnal oscillation, in their formation at night, and in reaching their peak intensity during early morning. Observations indicate southerly geostrophic wind to be a necessary ingredient. Heights of these simulated LLJs are also consistent with observations.

Acknowledgments. This work was supported by the Department of Energy under Contract 091575-A-Q1, with the Atmospheric Sciences Division of Pacific Northwest Laboratories, the National Science Foundation, and the Naval Research Laboratory. The computation for this work was performed at the North Carolina Supercomputing Center.

REFERENCES

Blackadar, A. K., 1957: Boundary layer wind maxima and their significance for the growth of nocturnal inversions. *Bull. Amer. Meteor. Soc.,* **38,** 283–290.

Bonner, W. D., 1968: Climatology of the low level jet. *Mon. Wea. Rev.,* **96,** 833–850.

Boybeyi, Z., and S. Raman, 1992: A three-dimensional numerical sensitivity study of convection over the Florida peninsula. *Bound.-Layer Meteor.,* **60,** 325–359.

Brook, R. R., 1985: The Koorin nocturnal low-level jet. *Bound.-Layer Meteor.,* **32,** 133–154.

Businger, J. A., J. C. Wyngaard, Y. Izumi, and E. F. Bradley, 1971: Flux-profile relationships in the atmospheric surface layer. *J. Atmos. Sci.,* **28,** 181–189.

Chen, T., and J. A. Kpaeyeh, 1993: The synoptic-scale environment associated with the low-level jet of the Great Plains. *Mon. Wea. Rev.,* **121,** 416–420.

Chen, Y., X. A. Chen, and Y. Zhang, 1994: A diagnostic study of the low-level jet during TAMEX IOP 5. *Mon. Wea. Rev.,* **122,** 2257–2284.

Clark, R. D., 1987: An observational and numerical study of the summertime, Great Plains low level jet. Ph.D. dissertation, University of Wyoming.

Deardorff, J. W., 1978: Efficient prediction of ground surface temperature and moisture, with inclusion of a layer of vegetation. *J. Geophys. Res.,* **83,** 1889–1903.

Doyle, J. D., and T. T. Warner, 1991: A Carolina coastal low-level jet during GALE IOP 2. *Mon. Wea. Rev.,* **119,** 2414–2428.

Fast, J. D., and M. D. McCorcle, 1990: A two-dimensional numerical sensitivity study of the Great Plains low-level jet. *Mon. Wea. Rev.,* **118,** 151–163.

Hoecker, W. H., 1963: Three southerly low-level jet systems delineated by the Weather Bureau special pibal network of 1961. *Mon. Wea. Rev.,* **91,** 573–582.

Holton, J. R., 1966. The diurnal boundary layer wind oscillation above sloping terrain. *Tellus,* **19,** 199–205.

Huang, C. Y., 1990: A mesoscale planetary boundary layer numerical model for simulations of topographically induced circulations. Ph.D. dissertation, North Carolina State University at Raleigh.

——, and S. Raman, 1989: An application of the *E–e* closure model to simulations of mesoscale topographic effects. *Bound.-Layer Meteor.,* **49,** 169–195.

——, and ——, 1990: Numerical simulations of cold air advection over the Appalachian Mountains and the Gulf Stream. *Mon. Wea. Rev.,* **118,** 343–362.

——, and ——, 1991a: Numerical simulation of January 28 cold air outbreak during ''GALE'' II, the model and sensitivity tests of turbulence closures. *Bound.-Layer Meteor.,* **55,** 381–407.

——, and ——, 1991b: Numerical simulation of January 28 cold air outbreak during ''GALE'' II, the mesoscale circulation and marine boundary layer. *Bound.-Layer Meteor.,* **56,** 51–81.

——, and ——, 1992: A three-dimensional numerical investigation of Carolina coastal front and the Gulf Stream rainband. *J. Atmos. Sci.,* **49,** 560–584.

Kraus, H., J. Malcher, and E. Schaller, 1985: A nocturnal low level jet during PUKK. *Bound.-Layer Meteor.,* **31,** 187–195.

Mahfouf, J.-F., E. Richard, and P. Mascart, 1987: The influence of soil and vegetation on the development of mesoscale circulations. *J. Climate Appl. Meteor.,* **26,** 1483–1495.

Nagata, M., and Y. Ogura, 1991: A modeling case study of interaction between heavy precipitation and a low-level jet over Japan in the baiu season. *Mon. Wea. Rev.,* **119,** 1309–1336.

Nicolini, M., K. M. Waldron, and J. Paegle, 1993: Diurnal oscillation of low-level jets, vertical motion, and precipitation: A model case study. *Mon. Wea. Rev.,* **121,** 2588–2610.

Parish, T. R., A. R. Rodi, and R. D. Clark, 1988: A case study of the summertime Great Plains low level jet. *Mon. Wea. Rev.,* **116,** 94–105.

Segal, M., R. Avissar, M. C. McCumer, and R. A. Pielke, 1988: Evaluation of vegetation effects on the generation and modification of mesoscale circulations. *J. Atmos. Sci.,* **45,** 2268–2292.

Stull, R. B., 1988: *An Introduction to Boundary Layer Meteorology.* Kluwer Academic, 666 pp.

Uccellini, L. W., 1980: On the role of upper tropospheric jet streaks and leeside cyclongenesis in the development on low-level jets in the Great Plains. *Mon. Wea. Rev.,* **108,** 1689–1696.

Wexler, H., 1961: A boundary layer interpretation of the low-level jet. *Tellus,* **13,** 369–378.